2022 IEEE 18th International Conference on Automation
Science and Engineering (CASE)
August 20-24, 2022. Mexico City, Mexico

2022 IEEE 18th International Conference on Automation Science and Engineering (CASE) | 978-1-6654-9042-9/22/$31.00 ©2022 IEEE | DOI: 10.1109/CASE49997.2022.9926715

Investigating Statistical Correlation Between Multi-Modality In-Situ Monitoring Data for Powder Bed Fusion Additive Manufacturing

Zhuo Yang
System Integration Division
Associate of National Institute of Standards and Technology
Gaithersburg, MD
zhuo.yang@nist.gov

M. Adnan
Institute of Manufacturing Information and Systems
National Cheng Kung University
Tainan, Taiwan (R.O.C)
ad.gujjar@yahoo.com

Yan Lu
System Integration Division
National Institute of Standards and Technology
Gaithersburg, MD
yan.lu@nist.gov

Prof. Fan-Tien Cheng
Institute of Manufacturing Information and Systems
National Cheng Kung University
Tainan, Taiwan (R.O.C)
chengft@mail.ncku.edu.tw

Prof. Haw-Ching Yang
Department of Electrical Engineering
National Kaohsiung University of Science and Technology
Kaohsiung 82445, Taiwan
hao@nkust.edu.tw

Milica Perisic
System Integration Division
Associate of National Institute of Standards and Technology
Gaithersburg, MD
milica.perisic@nist.gov

Yande Ndiaye
System Integration Division
Associate of National Institute of Standards and Technology
Gaithersburg, MD
ndeye.ndiaye@nist.gov

***Abstract*—In-situ measurements provide vast information for additive manufacturing process understanding and real-time control. Data from various monitoring techniques observe different characteristics of a build process. Fusing multi-modal in-situ monitoring data can significantly enhance process anomaly detection, part defect prediction, and build failure diagnosis, thus improving AM part quality control. This paper compares the powder bed fusion in-process observations from two types of AM in-situ monitoring, coaxial melt pool imaging, and layerwise imaging, and investigates the correlation between the two observations for a build of parts with multiple geometric features and scan patterns. All data were collected from an open architecture powder bed fusion AM testbed. Data analysis shows that both datasets exhibit significant statistical changes when new features are introduced during the build. However, further machine learning-based modeling indicates that statistical features extracted from the two data sets do not correlate very well. Discussions are provided on how the statistical analysis of the observations from the two modality monitoring system can be utilized for data fusion strategy development, especially toward improving process anomaly detection.**

Keywords—Additive Manufacturing, Laser Powder Bed Fusion, Statistical Analysis, Machine Learning

I. INTRODUCTION

The powder bed fusion (PBF) additive manufacturing (AM) process uses laser beam to form parts layer by layer [1]. Every layer is a thin slice with the shape defined by 3D models. Upon one layer is finished, the build platform is lowered by a layer thickness and a fresh coat of powder is spread. Then either one or a set of laser beams is applied to scan the build surface, melt and join the material. A multitude of motion control and parameter regulation are involved during this cyclic process. Various advanced monitoring systems are developed and embedded into PBF machines to measure process variables [2]. Popular in-situ sensors for PBF include infrared pyrometer, high-speed coaxial camera, layerwise tower camera, and Galvo encoder [3]. Since each individual sensing system captures only certain characteristics of the process physics, fusing multi-modal in-situ monitoring data is expected to significantly enhance process anomaly detection, part defect prediction, and build failure diagnosis, thus improving AM part quality control [4]. However, sensing systems of different modalities generate different in-process monitoring data in scale, resolution, sampling rate, and meta information. Hence it is not feasible to fuse the raw data directly. Instead, data fusion can extract features from in-process measurements. Correlations between registered features derived from different in-process sensing systems are useful information for data fusion. However, in-process measurements are commonly contaminated by noises, so it is necessary to quantify the impact of noises on the correlation [5, 6]. Identifying these hidden correlations may contribute to anomaly detection and decision making. This paper aims to investigate the correlation of multi-modality in-situ monitoring data for different geometric features using statistical analysis and machine learning methods.

Overhang is a critical geometric feature for PBF, since it involves different levels of structural support during powder melting and solidification [7]. Solid support from the previously solidified layer is desired for uniform material properties and acceptable part dimensions. However, a part with complex geometry is likely to have overhangs with various angles. Overhang is the term to describe the surface supported by non-molten powders [8]. The weaker strength of loose powder in the overhanging regions causes defects such as craggy surface (or 'dross'), lower density, and inferior geometric deviation [9]. The same laser settings do not necessarily create regular sized melt pools in overhang regions due to the different heat conductivity [10]. One confirmed message is that the overhang geometry has a critical impact on the melting process, which is verified using coaxial melt pool monitoring (MPM) images in many studies [11].

This work extends the investigation to another type of dataset - layerwise images (LWI) with a much larger field of view but lower resolutions, which provides an alternative way to capture the physical changes caused by geometric features such as overhang. Hence, two types of experimental data, coaxial MPM image and LWI data are involved in this. The co-axial high-speed camera is set up on the same optical path with the moving laser beam to consistently focus on melting spots. It is an ideal way to monitor the melt pool conditions at high frame rates and with resolutions of a few micrometers. With proper data registration techniques, each melt pool image and the pixels can be located accurately on the build platform [12]. LWI has a global view of the build platform, which provides a large-scale analysis for the entire layer [13]. For MPM, some studies have successfully approximated temperature based on the optical image pixel value. However, evidence implies that uncontrollable uncertainties present during an optical-temperature calibration [14, 15].

The authors' former research applied data registration and fusion techniques to combine multi-modality data for process state identification [13]. The preliminary result shows that in-situ monitoring data demonstrate different characteristics when new geometric features are introduced. Other related studies also show that surface roughness, porosity, and melt pool size can also affect the in-situ data [16, 17]. Since every sensing technique only observes certain aspects of the process physical phenomenon, the observability of the process state depends on how each type of in-situ data is correlated to the process state. However, the relationships between in-situ observations and the process state are hard to model and measure, we start with correlating different types of in-situ observations and using that knowledge for data fusion. This paper aims to investigate the correlations between different modalities by statistical analysis and data-driven model. The outcome constructs the foundation of AM real-time control strategy which is urgently needed for the AM community.

II. Experimental Design

This research is an experiment-orientated study. A PBF platform embedded in-situ monitoring system builds four identical 3D parts. The 3D part is designed with noticeable geometric features for experimental needs. Secondly, the raw data would be preprocessed and registered for statistical analysis. If the analytical result exhibits relevance of geometric features in both modalities, such machine learning models would be built to quantify the mathematical correlations. Sub-sections elaborate on the abovementioned steps.

A. *Experimental Platform*

Four 3D parts were created by the Additive Manufacturing Metrology Testbed (AMMT) at the National Institute of Standards and Technology (NIST). AMMT is a fully customized metrology instrument that enables flexible control and measurement of the Laser PBF process [2]. It equips the capability to realize precise laser beam control. In order to advance G-code, the digital commands that AMMT uses set precise laser beam position, laser beam power, and coaxial camera trigger every 10 µs [18]. More details about AMMT can be found in Lane et al, 2020.

B. *3D Part with Overhang*

This experiment creates four nominally identical parts within the same build on a wrought nickel alloy 625 (IN625) substrate that is cut to $100 \times 100 \times 12.5$ mm. All four parts have the same geometry: a bounding box $5 \times 9 \times 5$ mm, a 45º overhang feature, and a cylinder cavity. According to the original report, data collected from the four parts has similar statistical features such as mean and standard deviation [18]. Post-measurement shows minimum difference in size, surface roughness, and mechanical behavior between parts. For demonstrative purposes, this study only uses the data from one part. The material is mixed recycled and virgin IN625 powder. The build consists of 250 layers at 20 µm per layer. The build employs a constant speed (800 mm/s) constant power (195 W) stripe scan pattern with skywriting. More details can be found in Lane and Yeung 2020 [18]. The general scan direction is designed to rotate 90º every layer. Table 1 lists the properties of the scan pattern and the abbreviation used in this paper. A 'vertical' or 'horizontal' scan track means the scan track is oriented in the Y or X direction, respectively. 'from right to left' or 'from top to bottom' means the tracks are scanned sequentially in the X or Y direction.

Table 1. Description of the scan patterns used in this work

	Scan Pattern	**Name**
Layer 1, 5, 9…	Vertical scan track from right to left	V-R2L
Layer 2, 6, 10…	Horizontal scan track from top to bottom	H-T2B
Layer 3, 7, 11…	Vertical scan track from left to right	V-L2R
Layer 4, 8, 12…	Horizontal scan track from bottom to top	H-B2T

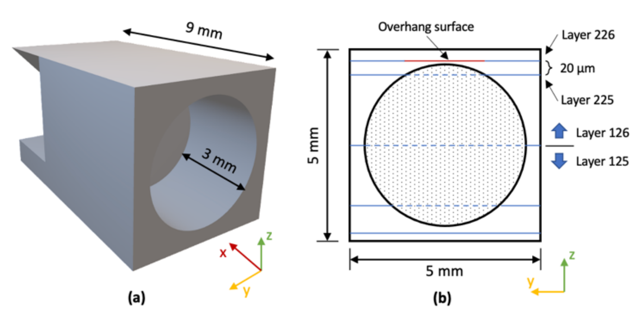

Figure 1. Part dimensions and key geometric features. (a) is the 3D view. (b) is cross-sectional view in YZ plane. It marks the key layers with new geometric features.

Figure 1 shows the designed part dimensions and the key geometric features. The part is 5 mm x 5 mm x 9 mm with 250 layers, where the layer thickness is 20 µm. The part has three regions.

A 3 × 5 × 9 mm region on one side with 45° overhang starts from Layer 51. Overhang edge in this region grows in the same size every layer. On the other side, a region of the same size has a cylinder cavity from Layer 25 to Layer 225. It aims to create a progressive overhang from Layer 126 to Layer 226. Since the layer thickness is the same at every layer, the overhanging level is different. Figure 2 shows an example of the three regions on one typical layer with all features.

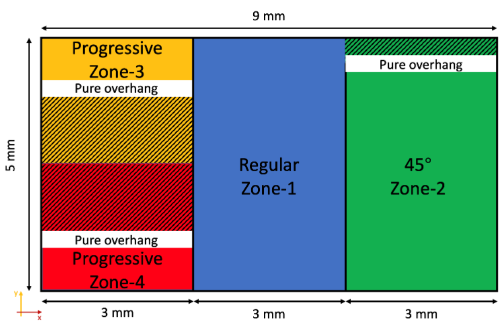

Figure 2. The three regions on one layer from the top view. Yellow and red color on the top-left represent the overhang region caused by the cylinder cavity. Blue represents the regular non-overhang region. Green represents the overhang created by the 45° slope. White area marks the overhang edges.

C. In-Situ Data

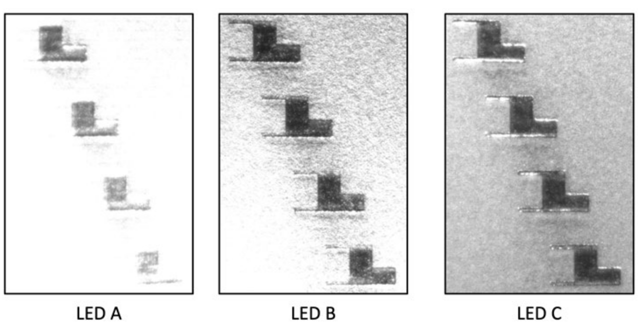

Figure 3. Four parts with the same geometry were built parallel on the build plate. Images captured by the same layer camera under different LED flash conditions. This experiment selects the data from the top part.

This experiment collects two types of in-situ data, LWI and MPM images. The experiment uses three LED flashlights shooting from different angles, namely LED A, B, and C, in the building chamber to capture the LWI at every layer. Once AMMT finishes scanning one layer, the tower camera would capture one image with each flashlight. A high-speed camera captures the coaxial MPM images with high frequency.

Figure 3 shows the LWI of one layer under three flash conditions. Note that the images shown in the figure have been processed and registered to correct the shape [13, 19]. As shown, images from LED A have oversaturated brightness. Later paragraphs would only discuss LED B and LED C.

Figure 4 shows two sample MPM images in the horizontal and vertical scan direction. The white spot located at the image center is the laser melting area named melt pool. MPM is 120 pixels by 120 pixels, where each pixel is 8 µm x 8 µm. The camera collects about 6000 MPM images at each layer. The accurate number of images depends on the scanning time. More than 1.5 million MPM data were collected and used in this work.

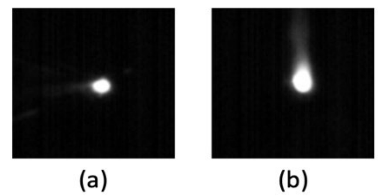

Figure 4. Sample MPM images.

III. Statistical Analysis For Mpm And Lwi

Data preprocessing is necessary to enable statistical analysis in both MPM and LWI. The first step is data preprocessing including image denoising and correcting distortion. Denoising an MPM image aims to remove the background low-intensity pixels and large spatters. This work deploys thresholding and autoencoder methods [19]. A low threshold grayscale value, 5-10, is usually sufficient for background noise removal. The autoencoder method is deployed to filter the MPM images to further remove the spatters, which usually have higher pixel values than the thresholding value. In some cases, the grayscale of high-temperature spatters is indistinguishable from the melt pools.

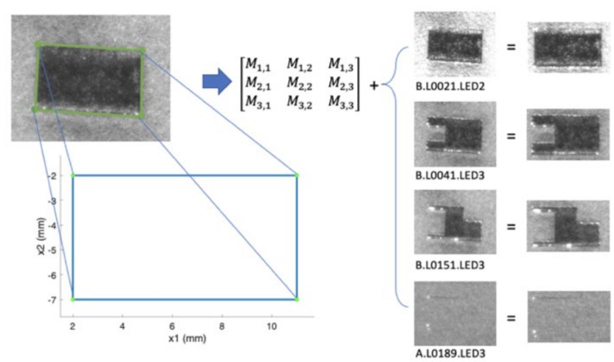

Figure 5. Part geometry in LWI is corrected by perspective image transformation.

Preprocessing for LWI data focuses on correcting the distortion and deformation associated with the relative camera position and the focus lens angle. The layer camera does not locate vertically to the build plate, nor is it a perfect pinhole. As a result, the raw LWI images have both distortion and deformation. Figure 5 shows the process of LWI image correction using a 4-point homography method. Four corner points of an early layer with a rectangular cross-section were used to derive the homography matrix [20]. Assuming that the distortion is identical for all the images because the tower camera is still during the build process, the homography matrix is then applied to all the LWI images to align the pixels to the real-world coordinates.

A. Statistical Feature Extraction

This study focuses on two statistical features of each modality. MPM analysis studies the average melt pool size and its standard deviation per layer. LWI analysis focuses on the layerwise grayscale average value and standard deviation. The statistical features are extracted for the overhang and regular regions separately. Note, regular region uses all the melt pools and the LWI pixels in the regular zone (blue in Figure 2). In fact, the majority area of the overhang zones actually are built on top of solidified material and have normal support conditions.

Figure 6 explains how this study distinguishes the pure overhang area from the overhang zones. The figure shows the cross-sectional view of a four layers example, where each bar represents one layer. Layer i to Layer i-2 all have a newly grown area on the right side. Under global view, the combined colored regions can be considered in an overhang zone. However, only the red areas directly contact the underneath raw powder with weak support. The layers on top of the red area start to rebuild the support immediately. After several layers, the support can recover near the normal level.

Figure 6. Both MPM and LWI only extract features of the pure overhang region. This study distinguished the area from each layer to purify the overhang effect.

Consequently, only the melt pools and pixels on the pure overhang area would be included in the statistical analysis. That demands the feature extraction to precisely trim the data to the area with the strongest overhang effect. This study distinguished the pure overhang area based on the pixel size in the corrected LWI images. It analyzes the data from 1 to 4 pixels, where is 0.0649 to 0.2596 mm. Similarly, melt pools within this range are included to calculate the layerwise and zone-specific average and stand deviation. Figure 7 shows an example of a maximum 4 pixels width.

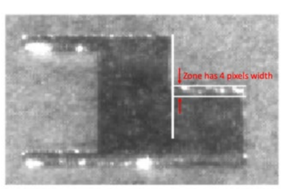

Figure 7. Overhang zone with 4 pixels width.

B. Statistical Analysis for MPM data

Figure 8 shows the average melt pool size of each layer for all four zones. The blue curve represents Zone-1 for the regular condition starts from Layer 1 to 250. Zone-2 for 45° overhang is in green starting from Layer 51. Yellow and red curves represent the progressive overhangs starting from Layer 126 to Layer 225. The only difference between Zone-3 and Zone-4 is that they are located at the two ends of the cylinder hole opening. Based on the result, Zone-1 has the largest and the most consistent melt pool size than other zones due to regular support from previous layers and consistent volume. The overhang zones have significantly smaller melt pools and the variation between layers is much larger.

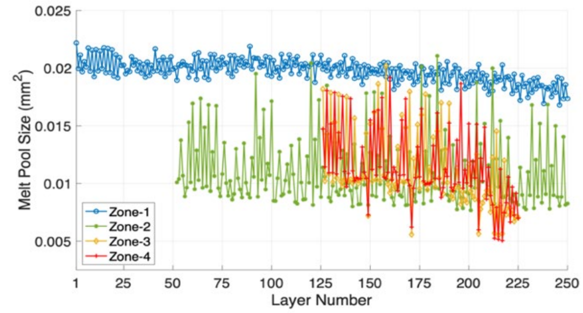

Figure 8. Comparison of melt pool size of all four zones. This chart shows the average melt pool size for all four zones.

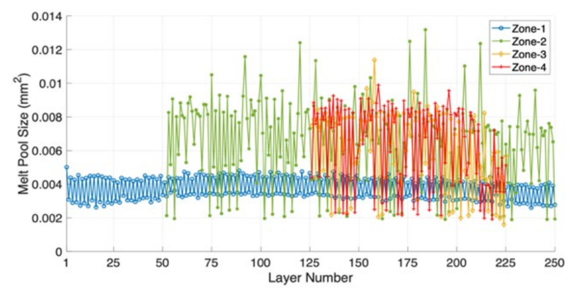

Figure 9. Comparison of melt pool size of all four zones. This chart shows the standard deviation of melt pool size for all four zones.

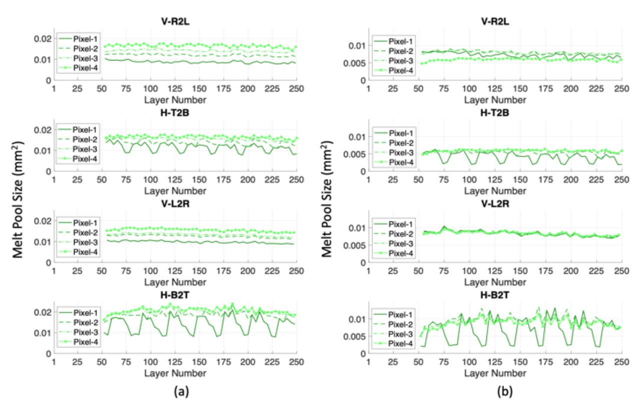

Figure 10. (a) Average melt pool size of Zone-2, separated by scan pattern. Melt pool size is increasing from Pixel-1 to Pixel-4. This indicates same energy tends to create a smaller melting surface area in severer overhang regions. Vertical scan is more consistent than horizontal scan. **(b)** Variation of melt pool size in Zone-2, separated by scan patterns. A severer overhang can cause larger melt pool uncertainty.

However, the layerwise standard deviation of the melt pool size seems opposite to the previous observation. Zone-1 stand deviation is significantly lower than any overhang zone. As shown in Figure 9, Zone-1 maintains the melt pool variation in a low and consistent range. However, Zone-2 to Zone-4 have a much wider range for standard deviation and the values seem more random.

Scan direction may also affects melting conditions since it determines how the laser beam pass the overhang zones. Figure 10 groups the layers based on the scan patterns listed in Table 1 for Zone-2. In this study, the part cross sections, regardless the layer number and the zone number, have longer length in y axis (3 mm) and significant shorter length in x axis (≤ 0.2596 mm). Consequently, the vertical scan pattern in the overhang zone has shorter scan duration than the horizontal scan pattern. The observations from these two figures verify this hypothesis. V-R2L and V-L2R are more similar than H-T2B and H-B2T in both layerwise average and layerwise standard deviation of the melt pool size. Specific to Pixel-1 in H-T2B and H-B2T, the curves have a periodic behavior every 25 layers. This might be caused by the combined effect of overhang growth and hatching center shifts.

Figure 11 shows the result of Zone-1 for comparison. The average melt pool size is generally higher than Zone-2 and the standard deviation is significantly lower. Horizontal scan pattern, H-T2B and H-B2T are more consistent than vertical scan according to their low variation in (b).

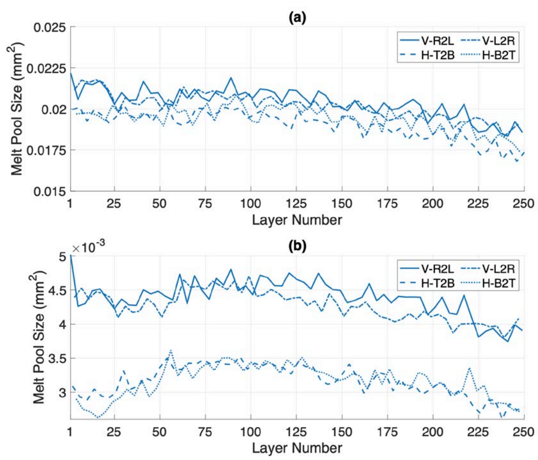

Figure 11. (a) shows the average melt pool size for Zone-1. (b) is the standard deviation. Legend marks the scan pattern.

C. *Statistical Analysis for LWI data*

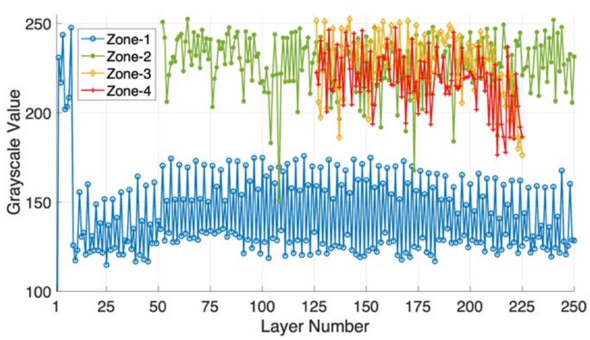

Figure 12. Comparison of average grayscale value of all four zones using LED B. Zone-1 has the lowest grayscale value.

Similarly, LWI data analysis reveals the grayscale differences between the overhang and non-overhang zones. This sub-section selects LWI data in Zone-2 using LED B and the result is shown in Figure 12. In general, Zone-1 has a significantly lower grayscale value than overhang zones. Note, that the first 10 layers have exposure issues that make the image almost saturated to pure white color.

Figure 13 shows the same comparison for the layerwise standard deviation of LWI image grayscale values. As observed in MPM, the standard deviation overturns the trend from the average value. Zone-1 has the largest standard deviation.

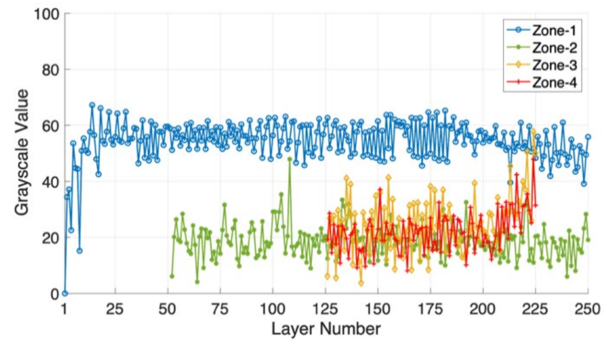

Figure 13. Comparison of the standard deviation of grayscale value of all zones using LED B. Legend marks the Zones.

Figure 14 (a) groupedd the layers based on scan patterns. Not like the melt pool size result, grayscale values from LWI seems not sensitive to the scan pattern. For all four patterns, the grayscale value is generally decreasing from width Pixel-1 to Pixel-4, though some layers have outstanding values. (b) shows the standard deviation of LWI grayscale is opposite to the average value. Pixel-1 now has the lowest variation. This value increases while the zone getting wider. Like Figure 15, the standard deviation seems not sensitive to scan pattern. All patterns show the same level of random errors.

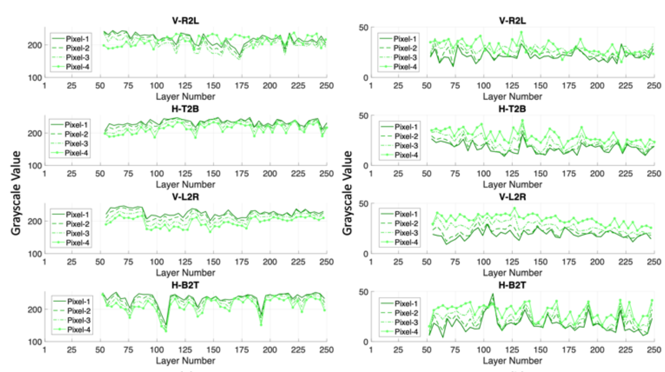

Figure 14. (a) Average grayscale values of Zone-2 of LED B. Closer to the overhang range, the average grayscale value tends to be higher regardless of the scan pattern. (b) Standard deviation grayscale values of Zone-2 using LED B. Lower variation observed on the edge of the overhang,

Similarly, Figure 15 compares the result of Zone-1 as a reference. The average grayscale value of all pixels in Zone-1 is generally lower than in Zone-2. However, the standard deviation is higher. Horizontal scan pattern, H-T2B and H-B2T are brighter than vertical scan according to their low variation in (a). Result for the first 10 layers is contaminated due to exposure issue. Brightness is saturated for these images. The issue is fixed after Layer 10. The contaminated result is included but would not be used for comparison.

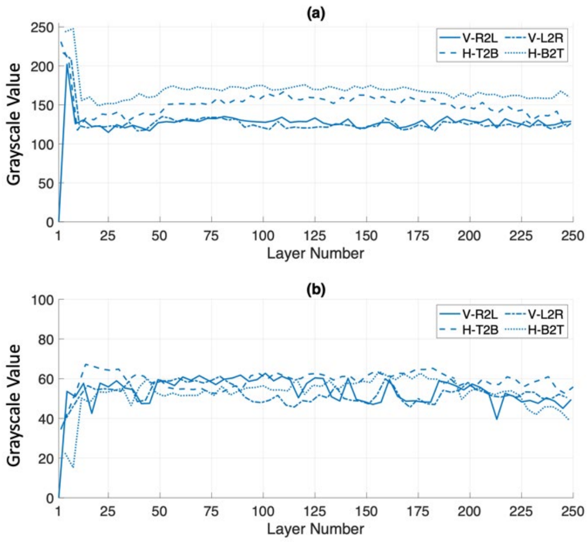

Figure 15. (a) shows the average grayscale value for all pixels in Zone-1. (b) shows the standard deviation.

D. Hypothesis

Preliminary analysis on MPM and LWI indicates that the overhang zones have significantly different statistical features from the regular zone. Though the detailed correlation between the features is still not fully understood, MPM and LWI simultaneously make noticeable reaction whenever overhang introduced to layer. It is worth to further investigate the correlations using machine learning techniques.

IV. Machine Learning Modeling For MPM And LWI Data

This study deploys backpropagation neural network (BPNN) for the correlation modeling, whereas the partial least square (PLS) regression is used as a reference model. Due to the multi-nature and non-linear relationship in the process of additive manufacturing, the BPNN algorithm is selected for the prediction case. BPNN performs well in understanding the complex relationship among the process parameters which helps to predict the accurate relationship between MPM and LWI quality index. The single hidden layer structure of the BPNN is utilized in the current case. The training and testing data are divided by 80% and 20%, respectively. The main purpose is to predict the LWI grayscale value based on the melt pool size. Furthermore, this work checks the effect of each offset pixel on LWI prediction to identify the best correction of MPI with flash conditions LED B and LED C.

The predicted LWI quality can be expressed as follows:

$$LWI(j,l)\hat{} = g(\textstyle\sum w(j)X(j,l) + B(j)) \quad (1)$$

$$X(j,l) = [F(I,l)] \quad (2)$$

$$g(x) = 1/(1+e^{(-x)}) \quad (3)$$

X(j,l) is the model input features of the model for the jth sample at l_{th} layer number. B(j,l) represents the bias of the model for the j_{th} sample of the l_{th} layer, F(I,l) is the features of the j_{th} sample at the lth layer, and g(x) is the activation function of the BPNN prediction model.

The final result of the mean absolute estimation error is essential to be less than a particular tolerance δ as presented in the subsequent equation [22]:

$$\sum_{j=1}^{m} |y(j,l) - y\hat{}(j,l)| \le \delta \quad (4)$$

The result section used the Zone-3 and Zone-4 to realize the purposed method's accuracy. All width from Pixel-1 to Pixel-4, and both LED B and LED C were studied.

A. Zone-1 Result

For Zone-1, LED C has a better correlation than LED B. The prediction model from training data layers includes Layer 61-100, Layer 111-200, and Layer 211-220. The testing data includes Layer 101-110 and Layer 201-210. Mean average error (MAE) is measured to evaluate the model result. MAE errors of the current model are 17.01 and 20.33 for BPNN and PLS prediction algorithms, correspondingly. Figure 16 demonstrates the model robustness toward the original trend prediction with enough accuracy. In figure 16, the y-axis (VM) represents the virtual metrology value. The range of RI is between 0 to 1, and the reliance index (RI) describes the difference between PLS and BPNN results. It compares the prediction values. The GSI is the global similarity index that checks the similarity between the input data and all historical sets of process data used for modeling.

B. Zone-2 Result

Based on the correlation analysis between input features and output of flash conditions, it was observed that LED C has a better correlation than LED B. This case predicts the LWI average grayscale of each layer. The input features to the prediction model are melt-pool average area, standard deviation, and scan pattern. MAE errors are 9.46 for BPNN and 9.41 for PLS. Figure 17 observes that the model prediction follows the LWI pattern well.

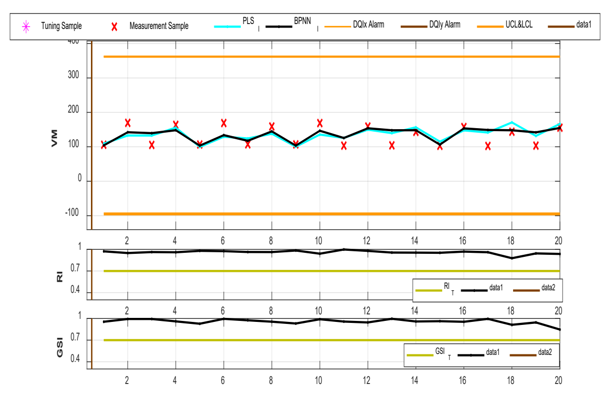

Figure 16. Zone-1 LWI prediction

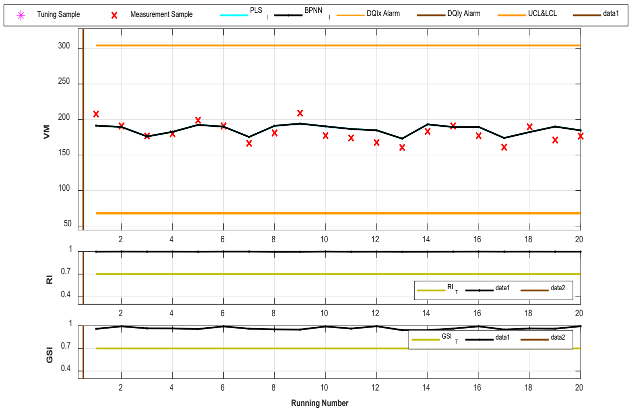

Figure 17. Zone-2 LWI prediction.

C. Offset Pixel-wise Comparison with LED B & C

In this case, we used all four pixel features of Zone-4 to check the LWI prediction accuracy. Table 2 and 3 list the MAE errors. It shows that pixel 3 and 4 have better prediction accuracy than pixel 1 and 2. It also indicates that pixel 3 and 4 are more sensitive to flash b. MAE are 7.10 for pixel 1 and 8.63 for pixel 4. As listed in the table, BPNN and PLS algorithms for flash b is better than the flash condition c. This analysis is also verified by the correlation of the scan pattern with flash conditions. A stronger correlation is observed in LED B rather LED C. In the case of Pixel 3 and 4, the prediction graph clearly shows that the model predicts the result close to real value and follows the trend very well also.

Table 2. LED B result.

Unit	MAE		Correlation	
	BPNN	PLS	MPI (scan pattern)	LWI (target)
Pixel(1)	10.73	10.78	0.396	
Pixel(2)	9.74	10.51	0.470	
pixel(3)	7.10	7.78	0.507	
Pixel(4)	8.63	9.16	0.521	

Table 3. LED C result.

Unit	MAE		Correlation	
	BPNN	PLS	MPI(scan pattern)	LWI (target)
Pixel(1)	19.04	19.13	0.075	
Pixel(2)	16.85	15.38	0.163	
Pixel(3)	11.46	10.74	0.199	
Pixel(4)	8.02	10.31	0.240	

V. DISCUSSION

This study presents the preliminary findings to investigate the future AM data fusion research direction. It aims to analyze multi-modality AM data under complex conditions. Sometimes, AM machine may have limit choice of in-situ monitoring sensors, especially for commercial AM machines. It is common that the machine can embed only one sensor to monitor the building process. If the sensors have completely different conclusion for the same problem, it is difficult to help the AM user to make any useful decision. Which sensor the user should trust? The good news is this study has verified the MPM and LWI can both identify the overhang occurrence with enough sensitivity. Based on our approach, there is no significant delay or noise observed for overhang features.

It seems that the machine learning models that try to create a point-to-point correlation between MPM and LWI are not as strong as expected. This is partially explainable based on the first principle that the MPM is representing the transient melting conditions, whereas the LWI is captured at the end of each layer. It is also presumably caused by the uncertainties in measurements. Each modality has its own noise, including both measurement error, and signal delay. These uncertainties cumulate in the input and output data for the model training. The findings from this paper suggest that point-to-point feature level data fusion (as defined in Figure 18) not working for the two modalities of the in-situ monitoring system. It might be more applicable if the data fusion is conducted at the decision level instead of the raw data level.

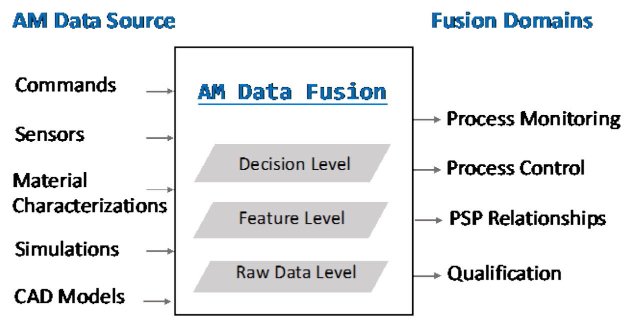

Figure 18. AM data fusion reference model [13]

A preliminary result using the Naive Bayes Classification model shows that overhang and non-overhang detection from MPM and LWI can be more effective to avoid false-positive defect detection [23]. Individual Bayes classifier is built according to a single data source. A soft voting system determines the final decision for geometric categories. It is more accurate than an individual classifier since each data source is sensitive to specific features without overlapping. It is also can help the users to better control the building process.

VI. SUMMARY

This study analyzed the statistical features from the in-situ monitoring data by two modalities. It is interesting to see both MPM and LWI are sensitive to the overhang features. Both melt pool size and grayscale value change abruptly when overhang occurs. Without knowing the geometry, AM users can identify the anomaly in the building process by analyzing the data. The low correlation between the datasets prevents the models to reach higher accuracy.

Further research is needed to justify the correlation by formulating the problem using observability analysis. Many existing works can provide useful information and benchmarks in such domain in AM specifications and model development [24-29]. The challenges are improving observability and reducing noises. By solving these problems, data fusion can be formed quantitatively. Data, meta-data, and related data schema can be found at the open AM data sharing platform, Additive Manufacturing Material Database [30].

DISCLAIMER

Certain commercial systems are identified in this paper. Such identification does not imply recommendation or endorsement by NIST; nor does it imply that the products identified are necessarily the best available for the purpose. Further, any opinions, findings, conclusions, or recommendations expressed in this material are those of the authors and do not necessarily reflect the views of NIST or any other supporting U.S. government or corporate organizations.

ACKNOWLEDGMENT

This work is supported by the “Intelligent Manufacturing Research Center (iMRC)” from The Featured Areas Research Center Program within the framework of the Higher Education Sprout Project by the Ministry of Education (MOE) in Taiwan.

REFERENCES

[1] Sun, S., Milan Brandt, and M. J. L. A. M. Easton. "Powder bed fusion processes: An overview." Laser Additive Manufacturing(2017): 55-77.

[2] Lane, B., Mekhontsev, S., Grantham, S., 2016, "Design, developments, and results from the NIST additive manufacturing metrology testbed (AMMT)," Solid Freeform Fabrication (SFF) Symposium, Anonymous pp. 1145-1160.

[3] Mani, Mahesh, Shaw Feng, Lane Brandon, Alkan Donmez, Shawn Moylan, and Ronnie Fesperman. *Measurement science needs for real-time control of additive manufacturing powder-bed fusion processes*. CRC Press, 2017.

[4] Lane, B., Grantham, S., Yeung, H., Zarobila, C., & Fox, J. (2017). Performance characterization of process monitoring sensors on the NIST Additive Manufacturing Metrology Testbed. In *2017 International Solid Freeform Fabrication Symposium*. University of Texas at Austin.

[5] Zhang, Shanshan, Brandon Lane, and Kevin Chou. "Powder thermal conductivity measurements in laser powder-bed fusion: an uncertainty study with sensitivity analysis." *Measurement Science and Technology* 32, no. 5 (2021): 055007.

[6] Lopez, Felipe, Paul Witherell, and Brandon Lane. "Identifying uncertainty in laser powder bed fusion additive manufacturing models." *Journal of Mechanical Design* 138, no. 11 (2016).

[7] H. Chen, D. Gu, J. Xiong, M. Xia, Improving additive manufacturing processability of hard-to-process overhanging structure by selective laser melting, J. Mater. Process. Technol. 250 (2017) 99-108.

[8] Chen, H., Gu, D., Xiong, J., 2017, "Improving Additive Manufacturing Processability of Hard-to-Process Overhanging Structure by Selective Laser Melting," Journal of Materials Processing Technology, 250pp. 99-108.

[9] Fox, J. C., Moylan, S. P., and Lane, B. M., 2016, "Effect of Process Parameters on the Surface Roughness of Overhanging Structures in Laser Powder Bed Fusion Additive Manufacturing," Procedia Cirp, 45pp. 131-134.

[10] Yeung, Ho., Lane, B., and Fox, J., 2019, "Part Geometry and Conduction-Based Laser Power Control for Powder Bed Fusion Additive Manufacturing," Additive Manufacturing, 30pp. 100844.

[11] Yang, Zhuo, Yan Lu, Brandon Lane, Jaehyuk Kim, Yande Ndiaye, and Sundar Krishnamruty. "Analyzing Remelting Conditions based on In-Situ Melt Pool Data Fusion for Overhang Building in Powder Bed Fusion Process." In *2021 International Solid Freeform Fabrication Symposium*. University of Texas at Austin, 2021.

[12] Lu, Y., Yang, Z., Kim, J., "Camera-Based Coaxial Melt Pool Monitoring Data Registration for Laser Powder Bed Fusion Additive Manufacturing," .

[13] Yang, Z., Lu, Y., Li, S., Li, "IN-PROCESS DATA FUSION FOR PROCESS MONITORING AND CONTROL OF METAL ADDITIVE MANUFACTURING," International Design Engineering Technical Conferences and Computers and Information in Engineering Conference, Anonymous ASME, .

[14] Lane, Brandon, Lars Jacquemetton, Martin Piltch, and Darren Beckett. "Thermal calibration of commercial melt pool monitoring sensors on a laser powder bed fusion system." *NIST Advanced Manufacturing Series* 100, no. 35 (2020): 100-35.

[15] Brandon Lane, Shawn Moylan, Ho Yeung, Jorge Neira, and Josephine Chavez-Chao. *Quasi-Static Position Calibration of the Galvanometer Scanner on the Additive Manufacturing Metrology Testbed*. US Department of Commerce, National Institute of Standards and Technology, 2020.

[16] Yang, Zhuo, Yan Lu, Ho Yeung, and Sundar Kirshnamurty. "3d build melt pool predictive modeling for powder bed fusion additive manufacturing." In *International Design Engineering Technical Conferences and Computers and Information in Engineering Conference*, vol. 83983, p. V009T09A046. American Society of Mechanical Engineers, 2020.

[17] Islam, M., Purtonen, T., Piili, H., Salminen, A., & Nyrhilä, O. (2013). Temperature profile and imaging analysis of laser additive manufacturing of stainless steel. Physics Procedia, 41, 835-842.

[18] Lane, B., and Yeung, H., 2020, "Process Monitoring Dataset from the Additive Manufacturing Metrology Testbed (AMMT): Overhang Part X4," Journal of Research of the National Institute of Standards and Technology, 125pp. 1-18.

[19] Lu, Yan, Zhuo Yang, Jaehyuk Kim, Hyunbo Cho, and Ho Yeung. "Camera-based coaxial melt pool monitoring data registration for laser powder bed fusion additive manufacturing." In *ASME International Mechanical Engineering Congress and Exposition*, vol. 84492, p. V02BT02A045. American Society of Mechanical Engineers, 2020.

[20] Huang, Yi-Ting, and Fan-Tien Cheng. "Automatic data quality evaluation for the AVM system." *IEEE Transactions on Semiconductor Manufacturing* 24.3 (2011): 445-454.

[21] H.-C. Yang, M. Adnan, C.-H. Huang, F.-T. Cheng, Y.-L. Lo, and C.-H.Hsu, “An intelligent metrology architecture with AVM for metal additive manufacturing,” IEEE Robot. Autom. Lett., vol. 4, no. 3, pp. 2886 2893, 2019.

[22] H.-C. Yang, C.-H. Huang, M. Adnan, C.-H. Hsu, C.-H. Lin, and F.-T. Cheng, “An online AM quality estimation Architecture- from Pool to layer,” IEEE Trans. Autom. Sci., vol. 18, iss.1, pp. 269–281, Jan. 2021.

[23] Zhuo Yang, Jaehyuk, Kim, Yan Lu, Ho Yeung, Brandon Lane, Albert Jones, Yande Ndiaye. A MULTIMODAL DATA-DRIVEN DECISION FUSION METHOD FOR PROCESS MONITORING IN METAL POWDER BED FUSION ADDITIVE MANUFACTURING. ASME IAM 2022

[24] Montazeri, Mohammad, and Prahalada Rao. "In-process condition monitoring in laser powder bed fusion (LPBF)." In *2017 International Solid Freeform Fabrication Symposium*. University of Texas at Austin, 2017.

[25] Gökhan Demir, Ali, Chiara De Giorgi, and Barbara Previtali. "Design and implementation of a multisensor coaxial monitoring system with correction strategies for selective laser melting of a maraging steel." *Journal of Manufacturing Science and Engineering* 140, no. 4 (2018).

[26] Montazeri, Mohammad, Abdalla R. Nassar, Christopher B. Stutzman, and Prahalada Rao. "Heterogeneous sensor-based condition monitoring in directed energy deposition." *Additive Manufacturing* 30 (2019): 100916.

[27] Furumoto, Tatsuaki, Takashi Ueda, Mohd Rizal Alkahari, and Akira Hosokawa. "Investigation of laser consolidation process for metal powder by two-color pyrometer and high-speed video camera." *CIRP Annals* 62, no. 1 (2013): 223-226.

[28] Wang, Feifan, Sepehr Fathizadan, Feng Ju, Kyle Rowe, and Nils Hofmann. "Print surface thermal modeling and layer time control for large-scale additive manufacturing." *IEEE Transactions on Automation Science and Engineering* 18, no. 1 (2020): 244-254.

[29] Wang, Qiyue, Wenhua Jiao, Peng Wang, and YuMing Zhang. "Digital twin for human-robot interactive welding and welder behavior analysis." *IEEE/CAA Journal of Automatica Sinica* 8, no. 2 (2020): 334-343.

[30] AMMD.nist.gov